

Dispersive modeling of breaking waves on a slope

Jihwan Kim^a, Geir K. Pedersen^a, Finn Løvholt^{a,b}, Randall J. LeVeque^c

^a*University of Oslo, Department of Mathematics, Oslo, Norway*

^b*Norwegian Geotechnical Institute, Oslo, Norway*

^c*University of Washington, Department of Applied Mathematics, Seattle, USA*

Abstract

The nonlinear shallow water model is widely used in the study of tsunami propagations, but an increasing number of studies are dedicated to the dispersion dynamics of tsunamis. If the wave dispersion becomes important, Boussinesq-type models are often used. In this work, a general purpose Boussinesq solver, BOUSSCLAW, is introduced for modeling fully non-linear dispersive tsunami propagation, taking into account inundation. In the BOUSSCLAW model, Boussinesq equations from the literature, based on the depth-averaged velocity and with enhanced dispersion properties, are implemented using a hybrid of the finite volume and finite difference methods. In order to validate BOUSSCLAW, numerical results are compared to the analytical solutions and laboratory experiments. Furthermore, the wave steepening and breaking motion is carefully scrutinized, and we demonstrate that the point of wave breaking may be wrongly identified in many of the commonly used Boussinesq models.

Keywords: Breaking wave, Boussinesq equation, finite volume method

1. Introduction

Tsunamis are often considered as long waves compared to the water depth, and long-wave models are consequently widely used in the study of their propagation and inundation. Through the use of numerical shock capturing techniques
5 for modeling the nearshore bore formation of the tsunami, *nonlinear shallow water* (NLSW) models did become the standard model for modeling tsunami

propagation and run-up, see e.g. (Titov and Synolakis, 1995; Imamura, 1996; Harig et al., 2008; Berger et al., 2011).

The NLSW models do not incorporate frequency dispersion, which may be
10 included by ascending in the hierarchy of long wave expansion to the Boussinesq
type equations. Numerical models based on Boussinesq type equations have
been used for idealized studies of wave processes since 1966 (Peregrine, 1966) and
additionally to simpler problems in coastal engineering in the following decades
(Brocchini, 2013). However, the accumulated effect of the frequency dispersion
15 for the wave propagation over the open sea is a function of propagation time
and the shape of the disturbance (Glimsdal et al., 2013), and may become
important for some tsunamis, in particular for landslide sources (Løvholt et al.,
2015). Dispersion may further be of importance, in combination with non-
linear effects, for the evolution of undular bores for tsunamis (Glimsdal et al.,
20 2013; Grue et al., 2008; Løvholt et al., 2008; Behrens and Dias, 2015). In
the last decades we have seen a development on long wave expansions and
their numerical formulations. In the 1990s the modeling with Boussinesq type
equations were vitalized by new formulations, in particular those of Madsen
and Sørensen (1992) and Nwogu (1993) which displayed improved dispersion
25 properties in comparison to the standard formulation of Peregrine (1967). Later
still more extensions and improvements have followed as described in the reviews
Madsen et al. (2003), Brocchini (2013) and Kirby (2016).

Boussinesq-type equations differ in mathematical structure from the NLSW
equations and do not inherit characteristics in the same simple form. Hence,
30 other strategies have been attempted for inclusion of wave breaking and post-
breaking motion in Boussinesq models. Schäffer et al. (1993) employed the
concept of the *surface roller*, first proposed by Svendsen (1984), which is vol-
ume of water passively riding at the bore front. Another way of incorporating
the breaking that was suggested by Kennedy et al. (2000) who included dif-
35 fusive terms in the momentum equation which was activated and deactivated
as a steepness measure crosses thresholds. The original steepness measure was
the temporal rate of surface elevation corresponding to a very steep solitary

wave. Later, Lynett (2006) investigated a variety of steepness measures and then identified that the surface steepness provides the least sensitive breaking
 40 threshold. Løvholt et al. (2013) similarly employed a diffusive model including transport terms, but pointed out that breaking wave Boussinesq models were prone to instabilities. Tissier et al. (2012) suggested a breaking decision model based on the surface roller, the maximal front angle and the Froude number. An alternative non-linear diffusive ad-hoc breaking term was suggested Matsuyama
 45 et al. (2007), based on their large scale experiments of the wave propagation of undular bores on various slope angles.

However, there is a natural desire to exploit the efficient and well established shock capturing framework for NLSW models also in a dispersive context. Hence, recently developed Boussinesq models are often based on hybrid numerical techniques such as use of approximate Riemann solvers combined with
 50 TVD limiters for the conserved variables, and finite differences for additional higher order terms (Erduran et al., 2005; Kim et al., 2009; Shiach and Mingham, 2009; Roeber et al., 2010; Dutykh et al., 2011; Shi et al., 2012). Among other models, this have led to the popular FUNWAVE-TVD and COULWAVE-TVD
 55 applications. For instance in Shi et al. (2012), Boussinesq terms are switched off the near-shore region where large amplitude-to-depth-ratios occur, implying that only NLSW terms remain in the shallowest region. This allows for a relatively robust treatment of the modeling of the post breaking phase. To this end, the $A/h = 0.8$ threshold suggested by (Shi et al., 2012) based on the Froude
 60 similarity analysis by Tonelli and Petti (2009), have in many ways become the standard for incorporating breaking in a feasible and practical way.

In this paper, we present a new hybrid Boussinesq type model BOUSSCLAW, of similar mould as FUNWAVE-TVD and COULWAVE-TVD. The emphasis is twofold. First, to present a careful validation of the model, both towards laboratory experiments and more general reference models. Second, we use the
 65 new model in comparison with a full potential reference model to explore how accurate the Boussinesq models can represent the wave evolution until the point of breaking. In the present example, we are finally able to demonstrate that

Boussinesq models may be employed to accurately model the near shore tsunami
70 propagation beyond the standard $A/h = 0.8$ threshold depth. Conversely, we
find that the use of the standard $A/h = 0.8$ threshold depth invokes a too early
formation of a breaking bore. This points out that that the breaking criteria
employed so far lacks generality.

This paper is organized as follows: In Section 2, the base model for the wave
75 equations is given and the numerical scheme is outlined, including a von Neuman
stability analysis. Sections 3 compares results from the BOUSSCLAW with the
analytic solutions and laboratory experiments. Section 3.4 discusses the wave
steepening and using a Boundary Integral Method (BIM) for solving the full
potential equations. In Section 4.1, we compare these results of pre-breaking
80 evolution with Boussinesq type models.

2. Model Description

Boussinesq-type equations are derived on the assumption that the ratio of
depth to wavelength, μ , is small. In addition one may assume that the ratio of
wave amplitude to depth, ϵ is small. Different kinds of long wave assumptions
85 are then generally characterized by relative errors in terms of these two param-
eters. Herein we will neither derive Boussinesq equation nor make the equations
dimensionless. Still, μ and ϵ will be used to indicate relative errors.

2.1. BOUSSCLAW - a new long wave model for tsunami propagation and run-up

In this work, a new numerical model, called BOUSSCLAW, is introduced. It is
90 an extension of GEOCLAW (Clawpack Development Team, 2016), and solves the
Boussinesq-type equations derived by The extened model is formulated in two
horizontal directions, but herein we focus on the description of plane waves for
simplicity. Tests and details on the performance with two horizontal directions
are found in Kim (2014).

95 The BOUSSCLAW model is a hybrid of the finite volume and finite difference
solvers with the fractional step technique. The GEOCLAW software is a part of

CLAWPACK (Clawpack Development Team, 2016) developed mainly by LeVeque (1997), George (2008) and Berger et al. (2011), which is designed to solve the nonlinear shallow water equations.

100 2.1.1. Boussinesq-type equations

Schäffer et al. (1993) derived Boussinesq-type equations with an addition of a Padé approximation of the linear dispersion relation. The equations read

$$H_t + (Hu)_x = 0, \quad (1)$$

$$(1 - D)[(Hu)_t] + \left(Hu^2 + \frac{g}{2}H^2\right)_x - gHh_x - Bgh^2(h\eta_x)_{xx} = 0, \quad (2)$$

where the operator D is defined as

$$D(w) = \left(B + \frac{1}{2}\right)h^2w_{xx} - \frac{1}{6}h^3\left(\frac{w}{h}\right)_{xx}, \quad (3)$$

for any $w(x, t)$. In the above equations $H(x, t)$ and $u(x, t)$ are the total flow depth and the depth averaged velocity of the water, respectively, $h(x)$ is the still water depth, $\eta(x, t)$ is the surface elevation, and thus $H(x, t) = h(x) + \eta(x, t)$. Moreover, g is the acceleration of gravity, and B is a dispersion parameter.

105 Madsen and Sørensen (1992) have chosen the parameter $B = 1/15$ from a Padé expansion of the linear dispersion analysis. When $B = 0$, this set of the Boussinesq-type equations approximately reduces to that of Peregrine (1967) as the linear dispersion relations are identical. However, unlike Peregrine's momentum equation the hydrostatic parts of (2) are written in a conservative
110 form. Moreover, some nonlinearity is introduced in the dispersion term for convenience. Even though (1), (2) and (3) do not constitute a fully nonlinear set of Boussinesq equations, inheriting relative errors of order μ^2 , $\epsilon\mu^2$, they do describe shoaling of solitary waves markedly better than, for instance, the Peregrine equations, as will be demonstrated in section 4.1.

115 The BOUSSCLAW model solves the Boussinesq-type equations (1) and (2) numerically with a hybrid combination of the finite volume and finite difference methods that will be explained in a moment. There have been several studies of this type of hybrid schemes. For example, see Tissier et al. (2011), Shi et al. (2012) and Dutykh et al. (2013).

Is it Schaeffer or M and S ?

To facilitate a fractional step method, as outlined below, we move the hydrostatic terms of (2) inside the $(1 - D)$ operator, while balancing with extra terms in the Ψ , to obtain

$$(1 - D)[(Hu)_t + \left(Hu^2 + \frac{g}{2}H^2\right)_x - gHh_x] = -\Psi(x, t), \quad (4)$$

where

$$\begin{aligned} \Psi(x, t) = & \left(B + \frac{1}{2}\right) h^2 ((Hu^2)_x + gH\eta_x)_{xx} \\ & - \frac{1}{6} h^3 \left(\frac{(Hu^2)_x + gH\eta_x}{h}\right)_{xx} - Bgh^2 (h\eta_x)_{xx}. \end{aligned} \quad (5)$$

2.1.2. Numerical scheme

The equations (1) and (4) are written in a form that conserves momentum to leading order in μ , but with the Ψ term as a pseudo source. Such equations may be solved by a *fractional step method* as described in LeVeque (2002), for instance. First, it is observed that (4) may be formally rewritten as

$$(Hu)_t = - \left\{ \left(Hu^2 + \frac{g}{2}H^2\right)_x - gHh_x \right\} - (1 - D)^{-1}\Psi(x, t), \quad (6)$$

At the first stage of the hybrid scheme, we integrate Hu over a time step taking into account all hydrostatic terms, namely those within the braces on the right hand side, and omitting the source terms involving Ψ . When this is combined with the continuity equation (1) this simply corresponds to advancing the shallow water equations one time step forward. To this end we employ GEOCLAW, a high-order accurate finite volume solver for the shallow water equations with adaptive mesh refinements.

In the second stage, we retain the new H value, but integrate Hu (essentially being the momentum density) further from the first stage by solving

$$(1 - D)[(Hu)_t] = -\Psi. \quad (7)$$

Since the differential operator D contains spatial derivatives, a systems of difference equations must then be solved.

The spatial and time discretization should be carefully chosen for the stability of the second stage. In our numerical scheme, the second order centered

scheme is used for the spatial discretization, and a four stage Runge-Kutta method is used for the time integration. The von Neumann stability analysis of this numerical scheme is outlined in Appendix A.

Suppose the spatial domain is divided into n grid cells with the spatial grid size Δx . Arrays of nodal values for flow depth and Hu , respectively, are defined as

$$\mathbf{H} = (H_1, H_2, \dots, H_n)^T,$$

$$\mathbf{M} = (H_1 u_1, H_2 u_2, \dots, H_n u_n)^T.$$

With time increment Δt the fourth order Runge-Kutta scheme can be written as follows,

$$\mathbf{M}^1 = \mathbf{M}, \quad \mathbf{M}^2 = \mathbf{M} + \frac{\Delta t}{2} \mathbf{S}^1, \quad \mathbf{M}^3 = \mathbf{M} + \frac{\Delta t}{2} \mathbf{S}^2, \quad \mathbf{M}^4 = \mathbf{M} + \Delta t \mathbf{S}^3, \quad (8)$$

where \mathbf{M}^k are intermediate value arrays and \mathbf{S}^k are correpondingly arrays for the time derivatives of Hu , obtained by solving

$$(I - \bar{D})\mathbf{S}^k = -\bar{\Psi}(\mathbf{H}, \mathbf{M}^k), \quad \text{for } k = 1, \dots, 4. \quad (9)$$

Here $\bar{\Psi}$ and \bar{D} represent centered spatial discretizations for the term Ψ and the operator D , respectively. These are given explitley below. Finally the value of \mathbf{M} at the new time level is obtained by

$$\mathbf{M}^+ = \mathbf{M} + \frac{\Delta t}{6} [\mathbf{S}^1 + 2\mathbf{S}^2 + 2\mathbf{S}^3 + \mathbf{S}^4]. \quad (10)$$

In (9), \bar{D} is a tri-diagonal $n \times n$ matrix with elements

$$\bar{D}_{i,i-1} = \frac{1}{\Delta x^2} \left[\left(B + \frac{1}{2} \right) h_i^2 - \frac{1}{6} \frac{h_i^3}{h_{i-1}} \right],$$

$$\bar{D}_{i,i} = \frac{1}{\Delta x^2} \left(-2B - \frac{2}{3} \right) h_i^2,$$

$$\bar{D}_{i,i+1} = \frac{1}{\Delta x^2} \left[\left(B + \frac{1}{2} \right) h_i^2 - \frac{1}{6} \frac{h_i^3}{h_{i+1}} \right].$$

Correspondingly, the i -th element of $\Psi(\bar{\mathbf{H}}, \mathbf{q})$ is

$$\begin{aligned}\bar{\Psi}_i = & \left(B + \frac{1}{2} \right) \frac{h_i^2}{2\Delta x^3} \left[\left(\frac{M_{i+2}^2}{H_{i+2}} - 2\frac{M_{i+1}^2}{H_{i+1}} + 2\frac{M_{i-1}^2}{H_{i-1}} - \frac{M_{i-2}^2}{H_{i-2}} \right) \right. \\ & \left. + g(H_{i+1}(\eta_{i+2} - \eta_i) - 2H_i(\eta_{i+1} - \eta_{i-1}) + H_{i-1}(\eta_i - \eta_{i-2})) \right] \\ & - \frac{1}{6} \frac{h_i^3}{2\Delta x^3} \left[\frac{M_{i+2}^2/H_{i+2} - M_i^2/H_i}{H_{i+1}} - 2\frac{M_{i+1}^2/H_{i+1} - M_{i-1}^2/H_{i-1}}{h_i} \right. \\ & \left. + \frac{M_i^2/H_i - M_{i-2}^2/H_{i-2}}{H_{i-1}} \right. \\ & \left. + g \left(\frac{H_{i+1}(\eta_{i+2} - \eta_i)}{H_{i+1}} - 2\frac{H_i(\eta_{i+1} - \eta_{i-1})}{h_i} + \frac{H_{i-1}(\eta_i - \eta_{i-2})}{H_{i-1}} \right) \right] \\ & - \frac{Bgh_i^2}{2\Delta x^3} (H_{i+1}(\eta_{i+2} - \eta_i) - 2H_i(\eta_{i+1} - \eta_{i-1}) + H_{i-1}(\eta_i - \eta_{i-2})),\end{aligned}$$

135 for $i = 1, 2, \dots, n$.

2.1.3. Additional numerical features

Following Shi et al. (2012) we may catch wave breaking in a heuristic fashion through invocation of a threshold $\epsilon_B := \eta/h = 0.8$ in BOUSSCLAW. When the threshold is reached, the wave breaking is supposed to be initiated, and
140 the dispersive terms are suppressed. At the breaking, the set of equations is locally switched to the shallow water equations for the corresponding leading wave, defines as stretching from the first nearshore elevation to the first negative trough following the crest that surpasses the threshold, , and the trailing waves are solved with the Boussinesq equations if the thresholds are not reached.

145 When a wave reaches the coastline, the coastline changes in time as the wave runs up the slope and recedes eventually. For the numerical simulations, it has been a challenge to compute the inundation correctly. At the coastline above the sea level, BOUSSCLAW switches to the NLSW solver of the GEOCLAW software, which can handle wet and dry states with the depth positivity property. Details
150 can be found in George (2008).

Friction terms are important for inundation on gentle slopes. For example, the Figure 7 shows that the run-up height is much reduced by the friction terms.

G: May have to modify according to new simulations.

BOUSSCLAW uses the Manning-type frictions as follows,

$$f_D = -\frac{gC_d^2 u |u|}{H^{5/3}},$$

where C_d is a Manning drag coefficient. Another parameter d^* needs to be chosen so that the water depth is set to $H = 0$ if the water depth is smaller than this threshold, $H < d^*$. Antuono et al. (2012) derived an approximate solution of the shoreline for the shallow water equations with the Chezy friction, and studied the effect of the frictional coefficient and the water depth tolerance. In this work, the parameter d^* is set to 10^{-4} . The dispersion terms of the Boussinesq equations imply an extended computational stencil as compared to that for the NLSW equations. To prevent this stencil from including non-wetted nodes and thereby produce irregularities and even instabilities, the dispersion terms are switched off when $H < Nd^*$, where the number N is set to 100 for the simulations herein.

2.2. Models for comparison

The performance of the Boussinesq model presented here is assessed by comparison with numerical results from a full potential flow model which is described in Løvholt et al. (2013) and references therein. The model is based on a boundary integral technique and is run with fully nonlinear solitary wave solutions as initial conditions. During shoaling and breaking this model can describe the evolution of a plunger, but breaks down when the plunger reaches the free surface. Hence, the potential flow results are used to determine the point of breaking due to shoaling and to evaluate the evolution of amplitude and wave shape of the current model until this point. Below we refer to the full potential model as the BIM (Boundary Integral Method) model.

Comparison with a pre-existing, fully nonlinear Boussinesq model is facilitated by the application of a Lagrangian model, described in Løvholt et al. (2013). Apart from the use of Lagrangian coordinates the equations employed in this model are similar to (1) and (2). They differ only concerning the nonlinearities in the dispersion terms and that the dispersion optimization terms

G: Jihwan,
check this

are added in a fully nonlinear fashion. Presently, the Lagrangian model has no established bore capturing facility and is hence valid only to the point of breaking. Results from this model will be referred to as 'Serre', even though the dispersion enhancement is invoked.

Results for the Peregrine-type Boussinesq equations are obtained by the GloBouss model. This is a dispersive tsunami propagation model which is based on Peregrine-type equations and discretization on a staggered grid. Further details are found in Løvholt et al. (2008).

For comparison also the version 2.1 of the FUNWAVE-TVD model by Shi et al. (2012) is used. The FUNWAVE-TVD model shares important features with BOUSSCLAW, employing a hybrid of the finite volume and finite difference scheme to solve the fully non-linear higher order dispersive Boussinesq model numerically. While we refer to Shi et al. (2012) for details, we briefly note that FUNWAVE-TVD is based the fully nonlinear Boussinesq equations of Chen (2006). The numerical spatial representation in FUNWAVE-TVD is MUSCL TVD scheme to discretize for the flux and first order terms, whereas a central finite difference scheme Wei et al. (1995a) is utilized for the higher order momentum terms. A Runge-Kutta scheme is employed for the time stepping.

3. Numerical Tests

3.1. Solitary wave propagation

In order to validate the numerical approach a solitary wave propagation is tested on a constant water depth. For the initial conditions, the analytic solitary wave solution of the Serre's equations is used since analytic solutions are unknown for the set (1) and (2). Solitary wave solutions to Serre's equations are given as

$$\begin{aligned}\eta(x, t) &= A \operatorname{sech}^2(\kappa(x - ct)), \\ u(x, t) &= c \frac{\eta(x, t)}{h},\end{aligned}\tag{11}$$

where

$$\kappa = \frac{\sqrt{3h}}{2A\sqrt{A+h}}, \quad \text{and} \quad c = \sqrt{g(A+h)}. \quad (12)$$

In this expression, A and h are constants which represent the wave amplitude and the undisturbed water depth respectively.

200 In Figure 1, snapshots from the BOUSSCLAW simulation are shown at $t = 0, 4, 8$ and 12 with $\Delta x = 0.1$. For the initial conditions, the solution (11) is used with $A = 0.2$, $h = 1$ and $g = 9.81$. The computational results are in good agreement with the analytic solutions concerning height, shape and propagation speed. The amplitudes decreases very gently as the wave propagates.

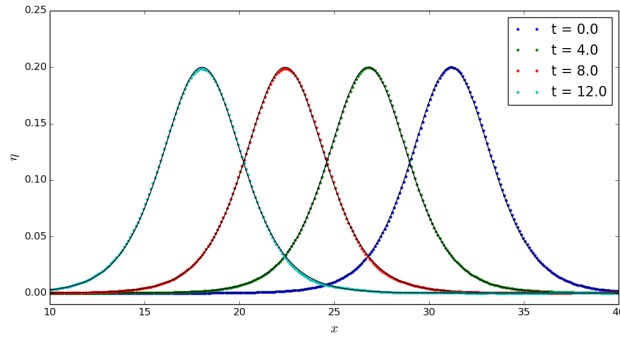


Figure 1: Snapshot of the analytic and computed solitary wave at $t = 0, 4, 8$ and 12 with $A/h = 0.2$. The wave propagates from right to left, and the analytic solutions are black solid lines.

The verically integrated wave energy densities for the shallow water equations and the Boussinesq equations are e_0 and $e_0 + e_1$, respectively, where

$$e_0 = \frac{1}{2} (g\eta^2 + H\bar{u}^2), \quad (13)$$

$$e_1 = \frac{1}{6} H^3 \bar{u}_x^2 + \frac{1}{2} H^2 h_x \bar{u} \bar{u}_x + \frac{1}{2} H h_x^2 \bar{u}^2. \quad (14)$$

205 Details are given in Madsen et al. (1997) and Appendix B. When the densities are integrated over the whole horizontal domain we obtain the corresponding total energies (per width), denoted as E_0 and E_1 .

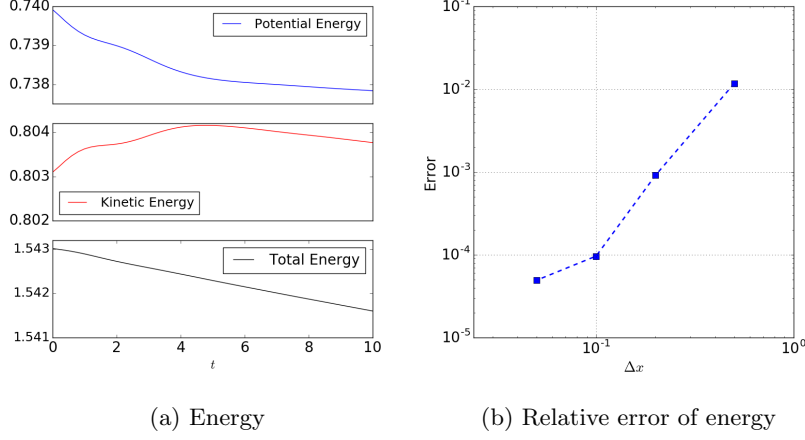


Figure 2: The energy of a solitary wave with $\Delta x = 0.2$ (left), and log-log plot of relative error at $t = 10$ for $\Delta x = 0.05, 0.1, 0.2$ and 0.5 (right).

In Figure 2a, the energy of the solitary wave is shown with $A/h = 0.2$ and $\Delta x = 0.2$. There are fluctuations both in the potential and kinetic energy that is evident when we zoom in, and the total energy decreases showing that the numerical procedure has dissipation. In Figure 2b, the relative error of the energy at $t = 10$,

$$Error = \frac{|E_{t=0} - E_{t=10}|}{|E_{t=0}|},$$

is shown for different Δx . For a solitary wave on a constant depth, the energy dissipation decreases with the grid increments.

210 3.2. Waves on a composite slope

A physical model was constructed at the Coastal Hydraulic Laboratory of the U.S. Army Corps of Engineers in order to address beach erosion and severe flooding problems Briggs et al. (1995). The model beach consists of three piecewise linear slopes of 1:53, 1:150, and 1:13 with a vertical wall at the shoreline
 215 as shown in Figure 3. In the laboratory, the wavemaker was located at 23.23 m. The gauge data from three cases are provided where the ratio A/h is equal to 0.038, 0.259 and 0.681 with $h = 21.8$ cm.

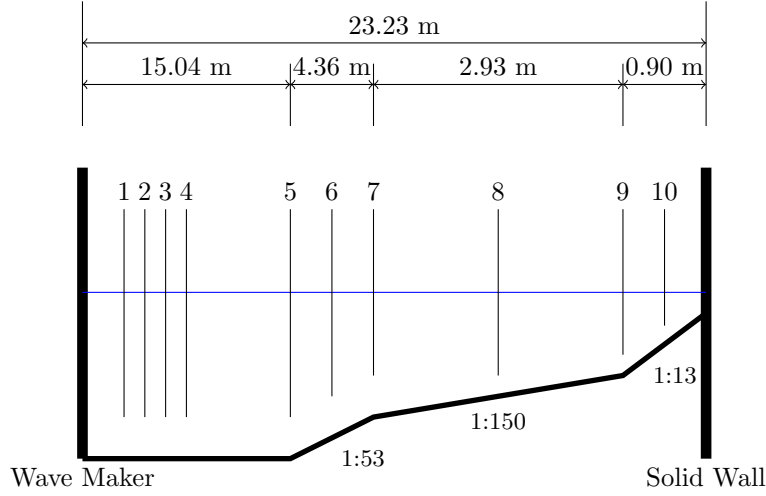


Figure 3: A sketch of the water tank

The second case with $A/h = 0.259$ has been compared with the numerical tests which employed 400 grid points. To specify the incoming wave from the left boundary, the data at Gauge 4 were used for the wave height, and the corresponding velocity (11) was applied.

In Figure 4, water surface elevations at gauges 5, 7 and 8 are shown. The simulated waves are in good agreement with the laboratory measurements. For the reflected waves, larger discrepancies are observed. The increased discrepancy occurs because the full interaction between the wave and the wall at the right boundary is less accurately captured. Friction forces influence the wave evolution along the shallow region near the right wall, but we have not included these in the present numerical simulation. A better fit may possibly be obtained by incorporating friction, however, tuning the friction models is not the scope of this work.

3.3. Shoaling and runup of solitary waves

In Figure 5, the initial set-up for a test is shown.

The set-up of the wave tank in the simulations follows the laboratory experiments by Synolakis (1987). The bathymetry of the wave tank is composed of a

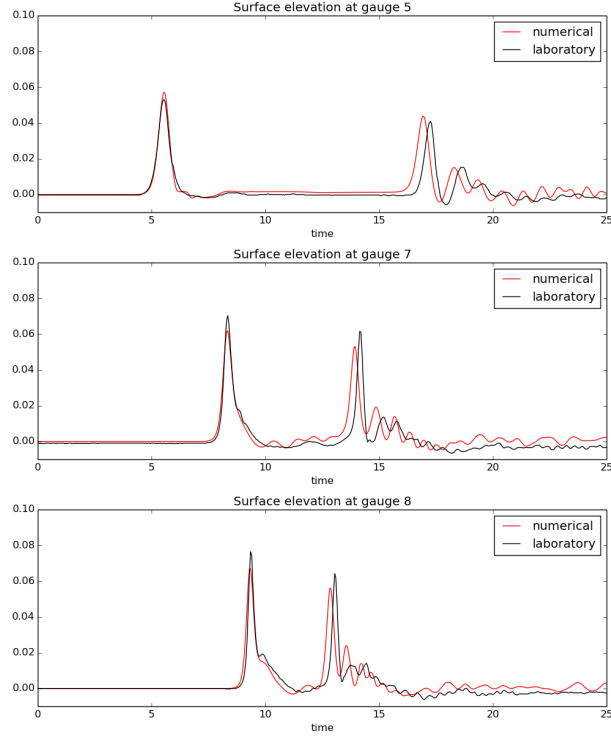


Figure 4: Water surface elevation at gauges 5,7 and 8 for $A/h = 0.269$ case.

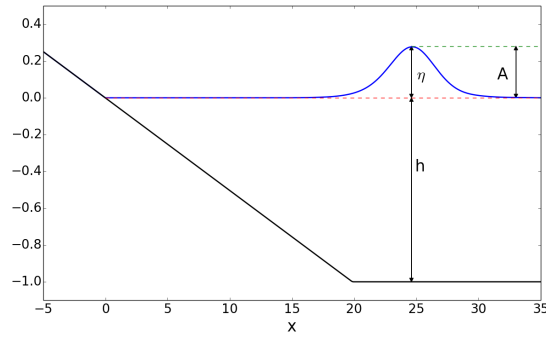


Figure 5: Set-up of a numerical test for shoaling and runup of solitary waves.

235 horizontal bottom and a uniform slope as shown in Figure 5. A solitary wave of
amplitude A is generated at the right end of the tank and propagates leftwards
to the beach.

We present the results using the non-dimensional time $t^* = t\sqrt{h/g}$ and non-dimensional space $x^* = x/h$. In the following, we drop the asterisks in the presentation of the results. In Synolakis (1987), $t = 0$ was defined as when the wave crest was a non-dimensional distance, L , from the toe of the slope, where

$$L = \sqrt{\frac{4A}{3h}} \operatorname{arccosh} \left(\frac{1}{0.05} \right).$$

However, at $t = 0$, the solitary wave has an elevation of 5% of its maximum at the toe of the beach, meaning that the slope has started to interact with the solitary wave. To avoid any such interaction obscuring our analysis, we instead place the initial solitary wave using equation (11) at $L + 5c$, where c is the shallow water wave celerity. In this way, the initial solitary wave has a negligible interaction with the slope when initialized.

3.3.1. Runup on a steep slope

On a 10° slope an incident solitary wave of amplitude $A/h = 0.3$ will not break until the end of the draw-down phase Grilli et al. (1997). Still, this may be a challenging task for Boussinesq type models (Løvholt et al., 2013). Runup on a 10° was investigated experimentally by Pedersen et al. (2013) who found a theoretical overshoot of roughly 20% in the maximum runup height. This was allotted to the viscous boundary layer on the beach and capillary effects. Moreover, the measurements showed that the boundary layer flow during runup was mostly laminar, albeit indications of transition was observed in the upper part of the swash tongue close to flow reversal. Hence, it is not appropriate to employ a Manning friction term and we compare the models without any bed friction, while leaving the experiments out. The agreement between the dispersive models are very good. Even though the fully nonlinear Serre model follows the BIM slightly better the BOUSSCLAW is also very close to full potential theory. For the given parameters the NLSW model yields premature breaking (see discussion on theoretical and observed breaking in Pedersen et al. (2013)) and a too high maximum runup height. The small wrinkles observed on the surface from the BOUSSCLAW are due to the switch to NLSW at the shore.

Check statement on wrinkles

Even though these small artifacts are enhanced by increasing resolution they do not give rise to instability or severe performance degradation for resolutions used. Instead, as demonstrated in figure ..., we obtain a solid grid convergence for tyhe BOUSSCLAW model. This is in sharp to contrast to observations for
 265 other models as presented in Løvholt et al. (2013).

3.3.2. Comparson with experiments on a breaking wave

Synolakis (1987) performed a series of laboratory expseriments for the run-up of solitary waves on uniform slopes. Here, we are interested in the breaking
 270 cases. One such example in Synolakis (1987) is a solitary wave of amplitude $A/h = 0.28$ approaching a slope of 1 : 19.85.

In Figure 6, the laboratory measurements are shown with the computational results from the BOUSSCLAW (in Boussinesq and NLSW mode) and the BIM models for $A/h = 0.28$ and a 1 : 19.85 slope at $t = 15$. The grid size Δx is 0.05
 275 in the following simulations unless stated otherwise. This is before the wave breaks and both BOUSSCLAW and the BIM model are in good agreement with the experiments.

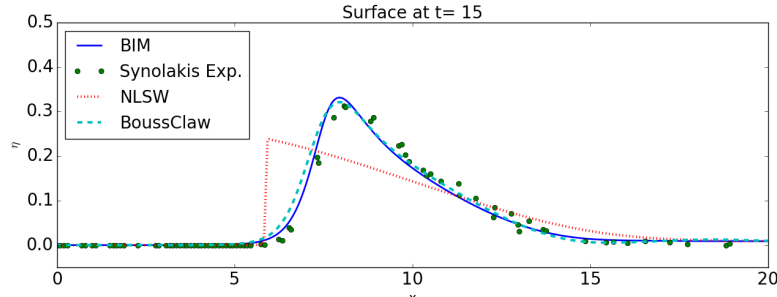


Figure 6: Comparison of the laboratory experiments, BIM, NLSW and BoussClaw at $t=15$ with $A/h = 0.28$ on a slope of 1 : 19.85.

The ratio of amplitude to depth, A/h , is about 2.01 at the break point. The potential flow model cannot be run much beyond the breaking points (until the attachment of the plunger only) and gives no information on the following bore
 280 propagation. In figure 7 we have compared the BOUSSCLAW model, with and

Add figure with stages in the runup, including BOUSSCLAW (without the threshold), NLSW, BIM and Serre. Add figure with shore-line history until maximum runup. Add figure with convergence of BoussClaw results. Add small table with maximum runup

without a Manning friction, with the experimental data. The agreement is good and the introduction of bed-friction even seem to match the truncated swash tongue of the experiments well. However, this may be a coincidence. Even though the wave has broken and some irregular flow features are introduced thereby, we have no evidence of the flow state being anywhere near turbulent, which is required for a quadratic bottom resistance to be appropriate. Capillary effects and experimental errors may also affect the comparison.

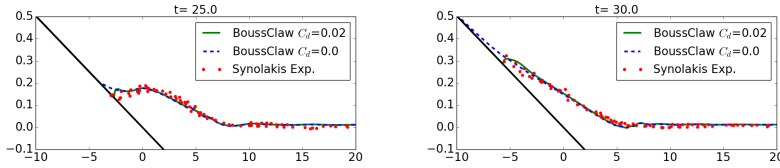


Figure 7: Comparison of experiments and BoussClaw results at $t=25$ and 30 .

4. Shoaling and breaking phenomena

4.1. Pre-breaking

Wei et al. (1995b) made computation of pre-breaking solitary wave shoaling with their fully nonlinear extension of Nwogu’s model, with full potential theory and the weakly nonlinear version of Nwogu’s model. They found that the fully nonlinear Boussinesq equations were superior to those of Nwogu in the later stages of the shoaling. In this subsection we will do a similar comparison for our models on the $1 : 19.85$ slope which was not included in the reference.

We use the set-up described in section 3.4 for the Boussinesq modeling of solitary waves on a slope. The BOUSSCLAW simulations are compared with those of other Boussinesq solvers, namely FUNWAVE (Shi et al., 2012), GLOBOUSS (Løvholt et al., 2010) and the Serre type formulation (Løvholt et al., 2013). As noted above, the original Serre’s equations are enhanced by adding the Schäffer et al. (1993) terms.

In Figure 8, snapshots from different numerical models are shown at $t = 16$, 18 and 20 . At the $t = 20$ there are no results from the BIM model as the wave

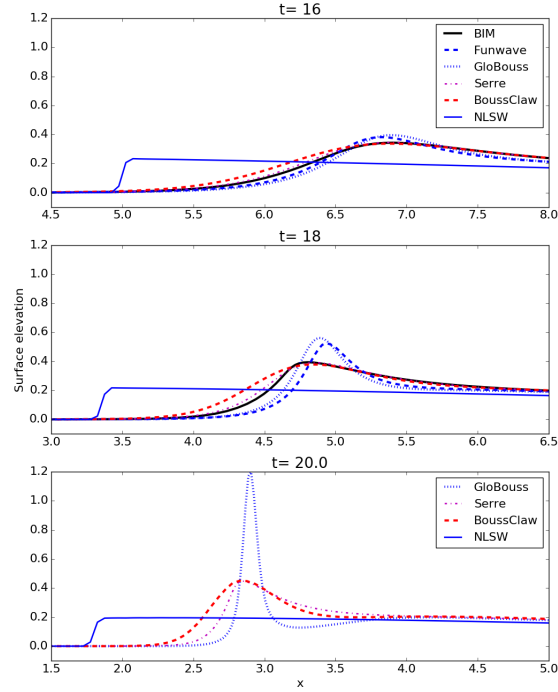


Figure 8: Snapshots of BIM, Serre, GLOBOUSS, BOUSSCLAW and FUNWAVE at $t = 16$, 18 and 20. The BOUSSCLAW is used with $B=1/15$, and the Peregrine's form is used for GLOBOUSS.

305 has broken. For the BOUSSCLAW, the parameter $B = 1/15$ is used, but the
 computational results are rather similar with $B = 0$ for this case. At $t=16$,
 the computational results from all the Boussinesq-type equations show similar
 results. The NLSW model, on the other hand, yields a premature breaking
 causing a too low amplitude. Moreover, the wave celerity is also over-estimated
 310 by the hydrostatic model. At $t=18$, some discrepancies are observed that can
 be split into two groups, and GLOBOUSS and FUNWAVE are similar while the
 BOUSSCLAW and the Serre results are similar. The wave amplitudes computed
 by the GLOBOUSS and FUNWAVE models, are more than 20 % larger than
 those from the BIM model. The wave amplitude continues to increase with

RJL: Why
 no BIM so-
 lution at $t =$
 20? G: could
 we include
 $t=19.1$ in-
 stead, with
 the BIM in
 place ?

315 GLOBOUSS simulations, and the difference from the BOUSSCLAW result becomes
larger at $t = 20$. The results from the Serre and BOUSSCLAW models clearly
more similar to those of the BIM model. Especially, the wave amplitudes are
correctly determined by these models. Our observations are in line with those
of Wei et al. (1995b).

320 4.2. Wave breaking and run-up

In the BIM model we may identify the onset of breaking according when
and where we first observe a vertical slope at the wave front. For an incident
amplitude of $A/h = 0.28$ on a $1 : 19.85$ slope, a vertical wave front is observed
at $x = 4.09$ and $t = 18.6$ with $A/h = 2.01$. When the crest in the BOUSSCLAW
325 simulation reaches $x = 4.09$, we find $A/h = 1.97$, the ratio of wave speed to
celerity (u/\sqrt{gH}) is 1.034 and maximum surface slope angle of 39.1° . If the
threshold $\epsilon_B = 0.8$ (see sec. 2.1.3) is used for the BOUSSCLAW model, the
threshold is reached at $t = 14.9$ when the peak of the wave is at $x = 8.03227$. In
the following, we explore the wave evolution with and without the application
330 of this threshold.

In Figure 9, snapshots are shown at $t=20, 25$, and 30 of the solutions from
BOUSSCLAW and NLSW with the Manning coefficient $C_d = 0.02$. We compared
the NLSW and BOUSSCLAW with $\epsilon_B = 0.8$ and without the threshold. At $t = 20$
the simulation with $\epsilon_B = 0.8$ has already been in NLSW mode for 5 time units
335 and the difference in the wave height from the full Boussinesq simulation is
significant. In fact, the threshold solution is closer to the NLSW solution. is
clearly observed.

At $t = 25$ and $t = 30$, the wave is running up the slope, and the difference
in the swash tongue is relatively small. While BOUSSCLAW simulation with
340 $\epsilon_B = 0.8$ is smooth at $t = 20$, irregularities are observed around $x = 8$ due
to the accumulated errors generated by the splicing of Boussinesq and NLSW
equations.

Other thresholds, u/\sqrt{gH} and the maximum frontal angle, are computed
for the wave breaking. Figure 10 shows ϵ_B , u/\sqrt{gH} and the maximum frontal

Are there
Synolakis
data for
 $t=20$?
J: Yes, I can
include it if
necessary

How does
this evolve?
Is it seen in
other paper?
J: I didn't
see this re-
sult in other
papers.

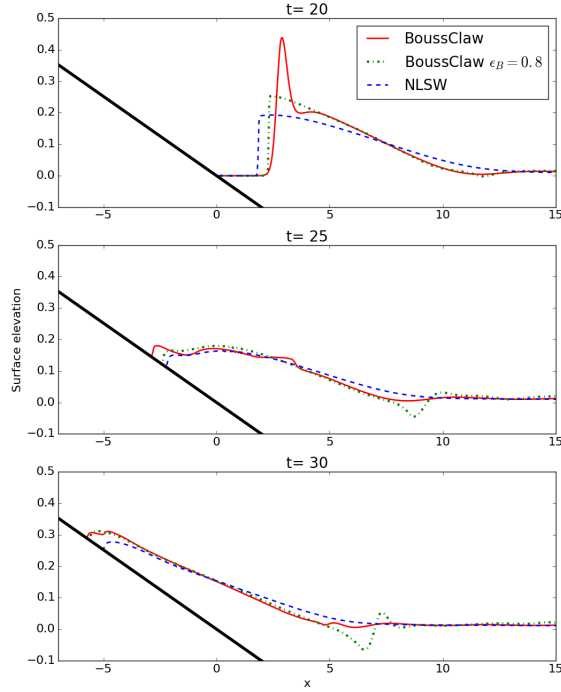


Figure 9: Comparison of BOUSSCLAW and NLSW with $\epsilon_B = 0.8$ at $t=20, 25$ and 30 . Fiction forces have been added with $C_d = 0.02$.

angle as a function of the crest location. The choice of the threshold should be determined based on the experiments, and thus the threshold can vary case by case as noted by Lynett (2006) and Matsuyama et al. (2007) for example.

4.3. Wave Energy

The integrated wave energies for the shallow water equations and Boussinesq equations are E_0 and $E_0 + E_1$ respectively, which are given in (13) and (14).

In Figure 11 the energy densities are depicted as functions of the crest location, x_c . In the left panel we observe that the E_0 is nearly constant for the shallow water equations until a shock is formed around $x_c = 13$. Thereafter, energy is quickly dissipated. In the BOUSSCLAW simulation with no threshold

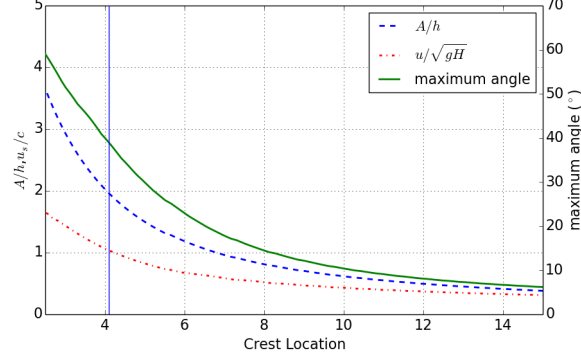


Figure 10: Plot of A/η , u_s/c and maximum angle of waves vs. crest location. BIM shows the wave break at $x = 4.09$.

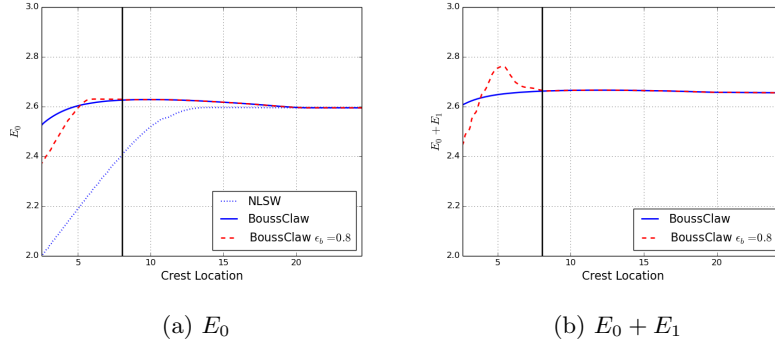


Figure 11: Energy plots of NLSW and BOUSSCLAW . The vertical line is at $x = 8.03227$ m where $\epsilon_B = 0.8$, and the governing equations are switched to the NLSW from the Boussinesq equations.

355 (right panel) $E_0 + E_1$ is nearly when the wave propagates in constant depth. On the deeper parts of the slope there is first a very moderate increase, then a very gentle reduction. This may be due to the absence of strict energy conservation in the Boussinesq equations in the first place. Close to the shoreline there is stronger, but still mild, energy dissipation. When the threshold $\epsilon_B = 0.8$ is
360 invoked there is no difference from the full Boussinesq solution until the the threshold is reached for $x_c = x_B = 8.03227$. Then, in fact, there is marked increase in $E_0 + E_1$ followed by a stronger reduction then for the full solution.

The increase is presumably a consequence of errors introduced by changing the governing equations from a Boussinesq to a NLSW type. After $x_c = x_B$ the hydrostatic energy measure, E_0 , may be appropriate in this case. The artificial energy maximum is then reduced and is only slightly higher than the general overshoot for E_0 and Boussinesq equations for $x_c > x_B$.

5. Conclusion

In the present paper we have presented a new Boussinesq type model, BOUSS-CLAW, for modeling fully non-linear dispersive tsunami propagation, taking also into account drying-wetting during inundation and withdrawal on the beach. BOUSSCLAW resembles much used general purpose models such as FUNWAVE-TVD and COULWAVE-TVD, but is based on a slightly simpler and more transparent set of governing equations, and has a slightly different numerical scheme. We have tested numerical implementation towards analytical solitary wave expressions as well as laboratory experiments.

Making use of the experiments of Synolakis (1987) enabled us to constrain a set of different long wave models, including BOUSSCLAW, as well as a full potential BIM reference model. Using the BIM, we were able to explore in detail the post-breaking behaviour, and to identify the point of breaking accurately. This was useful for determining the validity of the respective long wave models. First, we found that by using standard NLSW models, the point of breaking will be located too far offshore. Boussinesq models provide the opportunity of providing a more accurate description of the near shore propagation and shoaling. However, in current practise the Boussinesq terms are often omitted near shore through the $A/h > 0.8$ threshold criteria. As a consequence, the point of breaking may be misinterpreted also in Boussinesq type models.

In the present example, we investigated the near shore propagation over a relatively gentle shelf of $1/19.85$ slope, and in this case the actual onset of breaking occurred for $A/h \approx 2$, which is significantly later than what would be predicted in any standard approach (NLSW or Boussinesq). As demonstrated

G: Most appropriately e_0 should be integrated from the NLSW part, while $e_0 + e_1$ should be used elsewhere. How to conclude?

in this paper, the combined effects of non-linearities and dispersion influence the solution markedly, when accumulated to the point of breaking. It is noted that the artificial effect discovered would depend on the slope, and the $A/h = 0.8$ limited may well work better on a much gentler slope as it is primarily derived based on solitary wave evolution on constant depth. On the other hand, $1/19.85$ slope is already quite gentle, and the offset between the reference solution and Boussinesq models using this criteria may be even more pronounced for steeper slopes.

Temporary section: What to do

These are in addition to margin-notes.

1. Add references to introduction.
2. More figures for section 3.3; snapshots, shorelines maximum runup, convergence.
3. Grid increments must be described, somehow, for all results.
4. What to say about breaking performance ?
5. Old figures 9b, 10bc. Reinserted ?

Appendix A. Stability of the hybrid scheme

It is difficult to analyze the numerical stability for our full Boussinesq equations. To obtain some insight in the stability of the proposed hybrid numerical scheme, we thus consider a closely related, but simpler, equation, namely the linearized Benjamin-Bona-Mahony (BBM) equation (Benjamin et al. (1972))

$$u_t + cu_x = \frac{h^2}{6}u_{txx}, \quad (\text{A.1})$$

where $c = \sqrt{gh}$. This equation describes weakly dispersive, uni-directional waves in constant depth. The equation replaces the momentum equation, whereas no separate continuity equation is involved.

Following the steps of section 2.1.2, we rearrange the equation (A.1) as

$$(I - D)(u_t + cu_x) + Du_x = 0, \quad (\text{A.2})$$

where $D = \frac{h^2}{6} \partial_x^2$. The first step of hybrid scheme for this equation is integration of the advection equation

$$u_t + cu_x = 0, \quad (\text{A.3})$$

by the finite volume method. Then the Runge-Kutta method is applied to,

$$(1 - D)u_t + cDu_x = 0. \quad (\text{A.4})$$

which is the counterpart to (7).

If we use the centered spatial difference approximation of $O(\Delta x^2)$ accuracy on a regular grid we may employ a standard von Neumann analysis where we
415 calculate the growth of an harmonic mode over a single time step. Expressing the coefficients of the velocity array before the time step as $u_j = e^{i\xi j \Delta x}$ we then replace the coefficient of \mathbf{M}^q , defined in section 2.1.2, by $M_j^q = U_j^q = g^q e^{i\xi j \Delta x}$, where q is 1, 2, 3, 4 or +. Correspondingly, the coefficients of the \mathbf{S}^k array, which contains auxiliary, nodal values for u_t , is expressed $(S_j^k) = s^k e^{i\xi j \Delta x}$.

The stability of the first step, (A.3), is assured by the standard CFL criterion

$$\frac{c\Delta t}{\Delta x} < 1.$$

If we instead solve the NLSW equations, as in BOUSSCLAW, c must be replaced by the nonlinear characteristic velocity, which may lead to a more strict criterion. However, the method employed in the first step is not suited for a von Neumann stability analysis and we thus apply this technique to the second step only. Hence, we may put g^1 to unity, but it is preferable to retain it in the calculations. The Runge-Kutta scheme for time stepping, (8), may now be expressed as

$$g^2 = g^1 + \frac{\Delta t}{2} s^1, \quad g^3 = g^1 + \frac{\Delta t}{2} s^2, \quad g^4 = g^1 + \Delta t s^3, \quad (\text{A.5})$$

The discrete version of (A.4), which is the counterpart to (9) for the BBM equation reads

$$S_j^k - \frac{h^2}{6} \frac{S_{j+1}^k - 2S_j^k + S_{j-1}^k}{\Delta x^2} = -\frac{ch^2}{6} \frac{U_{j+2}^k - 2U_{j+1}^k + 2U_{j-1}^k - U_{j-2}^k}{2\Delta x^3},$$

which, inserted the harmonic expressions, implies

$$s^k = i \frac{\gamma}{\Delta t} g^k, \quad \gamma = c \Delta t \frac{2 \sin(\xi \Delta x) (1 - \cos(\xi \Delta x))}{6 \Delta x^3 h^{-2} + 2 \Delta x (1 - \cos(\xi \Delta x))}, \quad (\text{A.6})$$

where the Δt factors are included for convenience. The assembling of the intermediate values in the Runge-Kutta procedure, (10), now yields

$$g^+ = g^1 + \frac{\Delta t}{6} [s^1 + 2s^2 + 2s^3 + s^4]. \quad (\text{A.7})$$

By combination of (A.5) and (A.6) s^k and g^k , $k = 1..4$ can be calculated successively and combined in (A.7) to provide the value of g^+ ,

$$\begin{aligned} g^+(\gamma) &= \left(1 - \frac{1}{2}\gamma^2 + \frac{\gamma^4}{24} + \left(\frac{\gamma^3}{6} - \gamma\right)i\right) g^1 \\ |g^+(\gamma)|^2 &= \left(1 + \frac{1}{4}\gamma^4 + \frac{\gamma^8}{24^2} - \gamma^2 + \frac{\gamma^4}{12} - \frac{\gamma^6}{24} + \gamma^2 + \frac{\gamma^6}{36} - \frac{\gamma^4}{3}\right) |g^1|^2 \\ &= \left(1 - \frac{1}{72}\gamma^6 + \frac{1}{576}\gamma^8\right) |g^1|^2. \end{aligned}$$

Stability requires $|g^+(\gamma)/g^1| < 1$ which is equivalent to $|\gamma| < 2\sqrt{2}$. Moreover, it is easily seen that $\gamma < c\Delta t/\Delta x$. Hence, a sufficient condition for stability of the second step of the hybrid scheme is

$$\frac{c\Delta t}{\Delta x} < 2\sqrt{2}.$$

420 This is more relaxed than the CFL condition for the advection equation (A.3). Therefore, if the CFL condition is satisfied in the advection equation, the fractional step is always stable with the suggested numerical scheme.

Appendix B. Energy estimates and dissipation

Appendix B.1. Velocity field

To derive the energy estimates for the Boussinesq-type equations, we define the depth-averaged velocity as,

$$\bar{u} = \frac{1}{H} \int_{-h}^{\eta} u dz.$$

Then the velocity u can be expressed as $u = \bar{u} + u_1$ where $u_1 = O(\mu^2 \bar{u})$ and

$$\int_{-h}^{\epsilon\eta} u_1 dz = 0. \quad (\text{B.1})$$

Then the kinematic boundary condition at the bottom and zero divergence implies

$$w = -h_x \bar{u} - \bar{u}_x(z+h) + O(\mu^2).$$

425 *Appendix B.2. Energy integrals*

The potential energy density per horizontal area is

$$V = \int_{-h}^{\eta} g z dz = \frac{1}{2} g \eta^2 - \frac{1}{2} g h^2,$$

where the last term, $\frac{1}{2} g h^2$, is the equilibrium energy, while the first term is of order ϵ^2 relative to the first. The kinematic energy density has two contributions,

$$T = T_u + T_w; \quad T_u = \frac{1}{2} \int_{-h}^{\eta} u^2 dz, \quad T_w = \frac{1}{2} \int_{-h}^{\eta} w^2 dz.$$

where $T_w = O(\mu^2 T_u)$. For the horizontal part, T_u is

$$T_u = \frac{1}{2} \int_{-h}^{\eta} u^2 dz = \frac{1}{2} \epsilon^2 \int_{-h}^{\eta} \bar{u}^2 + 2\bar{u}u_1 + u_1^2 dz = \frac{1}{2} H \bar{u}^2 (1 + O(\mu^4)),$$

since \bar{u} is independent of z and $u_1 = O(\mu^2 \bar{u})$. The vertical part becomes

$$\begin{aligned} T_w &= \frac{1}{2} \int_{-h}^{\eta} h_x^2 \bar{u}^2 + 2h_x \bar{u} \bar{u}_x (z+h) + \bar{u}_x^2 (z+h)^2 dz \\ &= \frac{1}{2} H \left(h_x^2 \bar{u}^2 + H h_x \bar{u} \bar{u}_x + \frac{1}{3} H^2 \bar{u}_x^2 \right), \end{aligned}$$

where relative errors of order μ^2 are implicit. Thus the energy of a wave can be approximated as

$$e = (e_0 + e_1 + O(\mu^4 e_0))$$

where $e_1 = O(\mu^2 e_0)$ and

$$\begin{aligned} e_0 &= \frac{1}{2} (g \eta^2 + H \bar{u}^2), \\ e_1 &= \frac{1}{6} H^3 \bar{u}_x^2 + \frac{1}{2} H^2 h_x \bar{u} \bar{u}_x + \frac{1}{2} H h_x^2 \bar{u}^2. \end{aligned}$$

References

- V. V. Titov, C. E. Synolakis, Modeling of breaking and nonbreaking long-wave evolution and runup using VTCS-2, *Journal of Waterway, Port, Coastal, and Ocean Engineering* 121 (6) (1995) 308–316.
- 430 F. Imamura, Long-wave runup models, chapter Simulation of wave-packet propagation along sloping beach by TUNAMI-code, *World Scientific* 3 (1996) 4.
- S. Harig, Chaeroni, W. S. Pranowo, J. Behrens, Tsunami simulations on several scales, *Ocean Dynamics* 58 (5) (2008) 429–440, ISSN 1616-7228.
- M. J. Berger, D. L. George, R. J. LeVeque, K. T. Mandli, The GeoClaw software
435 for depth-averaged flows with adaptive refinement, *Adv. Water Res.* 34 (2011) 1195–1206.
- D. H. Peregrine, Calculations of the development of an undular bore, *J. Fluid Mech.* 25 (1966) 321–330.
- M. Brocchini, A reasoned overview on Boussinesq-type models: the interplay between physics, mathematics and numerics, *Proc. R. Soc.* 469 (2013) 20130496.
440
- S. Glimsdal, G. Pedersen, C. Harbitz, F. Løvholt, Dispersion of tsunamis: does it really matter?, *Nat. Hazards Earth Syst. Sci.* 13 (2013) 1507–1526.
- F. Løvholt, G. Pedersen, C. Harbitz, S. Glimsdal, J. Kim, On the characteristics of landslide tsunamis, *Phil. Trans. R. Soc. A* 373 (2053) (2015) 20140376.
- 445 J. Grue, E. N. Pelinovsky, D. Fructus, T. Talipova, C. Kharif, Formation of undular bores and solitary waves in the Strait of Malacca caused by the 26 December 2004 Indian Ocean tsunami, *J. Geophys. Res.* 113 (2008) C05008.
- F. Løvholt, G. Pedersen, G. Gisler, Oceanic propagation of a potential tsunami from the La Palma Island, *J. Geophys. Res.* 113 (2008) C09026.
- 450 J. Behrens, F. Dias, New computational methods in tsunami science, *Phil. Trans. R. Soc. A* 373 (2053) (2015) 20140382.

- P. A. Madsen, O. R. Sørensen, A new form of the Boussinesq equations with improved linear dispersion characteristics. Part 2. A slowly-varying bathymetry, *Coastal Engineering* 18 (3) (1992) 183–204.
- 455 O. Nwogu, Alternative form of Boussinesq equations for nearshore wave propagation, *Journal of waterway, port, coastal, and ocean engineering* 119 (6) (1993) 618–638.
- D. H. Peregrine, Long waves on a beach, *Journal of Fluid Mechanics* 27 (04) (1967) 815–827.
- 460 P. Madsen, H. Bingham, H. Schäffer, Boussinesq type formulations for fully nonlinear and extremely dispersive water waves: derivation and analysis, *Phil. Trans. R. Soc. Lond. A* 459 (2003) 1075–1004.
- J. T. Kirby, Boussinesq Models and Their Application to Coastal Processes across a Wide Range of Scales, *J. Waterw. Port, Coastal, Ocean Eng.* .
- 465 H. A. Schäffer, P. A. Madsen, R. Deigaard, A Boussinesq model for waves breaking in shallow water, *Coastal Engineering* 20 (3) (1993) 185–202.
- I. A. Svendsen, Mass flux and undertow in a surf zone, *Coast. Eng.* 8 (1984) 347365, doi:10.1016/0378-3839(84)90030-9.
- A. B. Kennedy, Q. Chen, J. T. Kirby, R. A. Dalrymple, Boussinesq modeling of wave transformation, breaking, and run-up. Part I: 1D., *J. Waterw., Port, Coast., Ocean Engrg.* 126 (1) (2000) 39–47.
- 470 P. J. Lynett, Nearshore wave modeling with high-order Boussinesq-type equations, *Journal of Waterway, Port, Coastal, and Ocean Engineering* 132 (5) (2006) 348–357.
- 475 F. Løvholt, P. Lynett, G. K. Pedersen, Simulating run-up on steep slopes with operational Boussinesq models; capabilities, spurious effects and instabilities, *Nonlin. Processes Geophys.* 20 (2013) 379–395.

- M. Tissier, P. Bonneton, F. Marche, F. Chazel, D. Lannes, A new approach to handle wave breaking in fully non-linear Boussinesq models, Coastal Engineering 67 (2012) 54–66.
- 480 M. Matsuyama, M. Ikeno, T. Sakakiyama, T. Takeda, A study of tsunami wave fission in an undistorted experiment, Pure and Applied Geophysics 164 (2-3) (2007) 617–631.
- K. Erduran, S. Ilic, V. Kutija, Hybrid finite-volume finite-difference scheme for the solution of Boussinesq equations, Int. J. for Num. Meth. in Fluids 49 485 (2005) 1213–1232.
- D.-H. Kim, P. Lynett, S. Socolofsky, A depth-integrated model for weakly dispersive, turbulent, and rotational flows, Ocean Modelling 27 (2009) 198–214.
- J. B. Shiach, C. G. Mingham, A temporally second-order accurate Godunov-type scheme for solving the extended Boussinesq equations, Coast. Eng. 56 490 (2009) 3245.
- V. Roeber, K. F. Cheung, M. H. Kobayashi, Shock-capturing Boussinesq-type model for nearshore wave processes, Coastal Engineering 57 (2010) 407423.
- D. Dutykh, T. Katsaounis, D. Mitsotakis, Finite volume schemes for dispersive wave propagation and runup, J. Comput. Phys. 230 (2011) 30353061.
- 495 F. Shi, J. T. Kirby, J. C. Harris, J. D. Geiman, S. T. Grilli, A high-order adaptive time-stepping TVD solver for Boussinesq modeling of breaking waves and coastal inundation, Ocean Modelling 43 (2012) 36–51.
- M. Tonelli, M. Petti, Hybrid finite volume–finite difference scheme for 2DH improved Boussinesq equations, Coastal Engineering 56 (5) (2009) 609–620.
- 500 Clawpack Development Team, Clawpack software, URL <http://www.clawpack.org>, version 5.3.1, 2016.
- J. Kim, Finite volume methods for Tsunamis generated by submarine landslides, Ph.D. thesis, University of Washington, 2014.

- 505 R. J. LeVeque, Wave propagation algorithms for multidimensional hyperbolic systems, *Journal of Computational Physics* 131 (2) (1997) 327–353.
- D. L. George, Augmented Riemann solvers for the shallow water equations over variable topography with steady states and inundation, *Journal of Computational Physics* 227 (6) (2008) 3089–3113.
- 510 M. Tissier, P. Bonneton, F. Marche, F. Chazel, D. Lannes, Serre Green-Naghdi modelling of wave transformation breaking and run-up using a high-order finite-volume finite-difference scheme, *Coastal Engineering Proceedings* 1 (32) (2011) 13.
- D. Dutykh, T. Katsaounis, D. Mitsotakis, Finite volume methods for unidirectional dispersive wave models, *International Journal for Numerical Methods in Fluids* 71 (6) (2013) 717–736.
- 515 R. J. LeVeque, *Finite volume methods for hyperbolic problems*, vol. 31, Cambridge university press, 2002.
- M. Antuono, L. Soldini, M. Brocchini, On the role of the Chezy frictional term near the shoreline, *Theoretical and Computational Fluid Dynamics* 26 (1-4) 520 (2012) 105–116.
- Q. Chen, Fully nonlinear Boussinesq-type equations for waves and currents over porous beds, *J. of Eng. Mech., ASCE* 132 (2) (2006) 220–230.
- G. Wei, J. T. Kirby, S. T. Grilli, R. Subramanya, A fully nonlinear Boussinesq model for surface waves. Part 1. Highly nonlinear unsteady waves, *J. Fluid Mech.* 294 (1995a) 71–92.
- 525 P. A. Madsen, O. Sørensen, H. Schäffer, Surf zone dynamics simulated by a Boussinesq type model. Part I. Model description and cross-shore motion of regular waves, *Coastal Engineering* 32 (4) (1997) 255–287.
- 530 M. Briggs, C. Synolakis, U. Kanoglu, D. Green, Runup of solitary waves on a vertical wall, *Costal Hydraulics Laboratory*, URL <http://chl.erdcl.usace.army.mil/chl.aspx?p=s&a=Projects;36>, 1995.

- S. Grilli, I. Svendsen, R. Subramanya, Breaking Criterion and Characteristics for Solitary Waves on Slopes, *J. Waterw. Port, Coastal, Ocean Eng.* 123 (3) (1997) 102–112.
- G. K. Pedersen, E. Lindstrøm, A. F. Bertelsen, A. Jensen, D. Laskovski, G. Sælevik, Runup and boundary layers on sloping beaches, *Physics of Fluids* 25 (2013) pp. 23, doi: 10.1063/1.4773327.
- C. E. Synolakis, The runup of solitary waves, *Journal of Fluid Mechanics* 185 (1987) 523–545.
- G. Wei, J. T. Kirby, S. T. Grilli, R. Subramanya, et al., A fully nonlinear Boussinesq model for surface waves. Part 1. Highly nonlinear unsteady waves, *Journal of Fluid Mechanics* 294 (7) (1995b) 71–92.
- F. Løvholt, G. Pedersen, S. Glimsdal, Coupling of Dispersive Tsunami Propagation and Shallow Water Coastal, *Open Oceanography Journal* 4 (2010) 71–82.
- T. B. Benjamin, J. L. Bona, J. J. Mahony, Model equations for long waves in nonlinear dispersive systems, *Philosophical Transactions of the Royal Society of London A: Mathematical, Physical and Engineering Sciences* 272 (1220) (1972) 47–78.